Self-Reference Broadband Local Wavenumber Estimation (SRB-LWE) for Defect Assessment in Composites

Joost Segers[1#], Saeid Hedayatrasa[1,2], Gaétan Poelman[1], Wim Van Paepegem[1] and Mathias Kersemans[1#]

[1] Mechanics of Materials and Structures (UGent-MMS), Department of Materials, Textiles and Chemical Engineering (MaTCh*)*, Ghent University, Technologiepark-Zwijnaarde 46, 9052 Zwijnaarde, Belgium

[#] Corresponding authors: Joost.Segers@ugent.be, Mathias.Kersemans@ugent.be

[2] SIM Program M3 DETECT-IV, Technologiepark-Zwijnaarde 48, B-9052 Zwijnaarde, Belgium

Abstract

Local wavenumber estimation (LWE) applied to a full wavefield response is a powerful approach for detecting and characterizing defects in a composite structure. However, the narrowband nature of the traditional LWE techniques brings several challenges for application on actual test cases.

This study proposes a self-reference broadband version of the LWE technique. The broadband vibrations are injected using low-power piezoelectric actuators (sine sweep signal) or using pulsed laser excitation in the thermoelastic regime. The out-of-plane velocity response of the surface is recorded using an infrared scanning laser Doppler vibrometer. The dispersive Lamb wave behavior, corresponding to the damage-free base material, is identified from the broadband vibrational response. Using the identified dispersion curves (i.e. self-reference approach), a Lamb mode passband filter bank in the wavenumber-frequency domain is constructed. Searching for the maximum bandpower density in function of the assumed material thickness provides a robust estimate of the effective local thickness of the tested component, and as such yields a detection and evaluation of damage.

The performance of the self-reference broadband LWE algorithm is demonstrated on aluminum plates with various flat bottom holes, as well as on cross-ply CFRP aircraft components with a stiffener disbond and barely visible impact damage. Compared to the traditional narrowband LWE approaches, the proposed self-reference broadband LWE method allows a higher level of automation, removes the need for a priori knowledge on the material and/or defect properties, and results in an improved characterization of defects.

Keywords

Composites; Non-destructive testing (NDT); Self-reference Broadband Local Wavenumber Estimation; Depth quantification; Scanning laser Doppler vibrometry; Guided waves

1. Introduction

Layered fiber reinforced polymer materials, or composites, are used as the base material for a large variety of structural components. The composite‘s high specific stiffness and strength, and design flexibility, allow to produce strong lightweight components. On the other hand, composites are susceptible to internal defects that may result from the production process or may be formed during the operational lifetime. As a result, non-destructive testing (NDT) is required to find and quantify these internal defects and thereby prevent the unexpected failure of the composite parts [1].

Composite components are often large and relatively thin-walled (order of mm's) panels or shells. This makes the use of NDT methods based on guided elastic waves, or Lamb waves, highly interesting. Depending on (i) the excitation frequency, (ii) the component's thickness and (iii) the full material's stiffness tensor, specific Lamb wave modes, or guided wave modes, are found to propagate in the component [2]. In correspondence with the displacement distribution through the thickness, the modes are classified as 'symmetric (S)' or 'anti-symmetric (A)' and are assigned a specific order. Each mode has a unique dispersion behavior that is characterized by the wavenumber *k* (i.e. inverse of the spatial wavelength, expressed in m^{-1}) in function of the temporal frequency *f*. The monitoring of the guided waves allows to detect defects in the medium because the characteristics of the guided waves depend on the characteristics of the medium (i.e. the composite component). The frequency of guided waves used for non-destructive inspection of thin-walled composite components is typically in the 50 to 500 kHz range.

In order to perform a non-destructive inspection using guided wave analysis, the guided waves have to be excited and afterwards recorded. Accurate and baseline-free defect detection is achieved through full wavefield monitoring of the excited waves. Such a full wavefield dataset can be obtained in multiple ways. One could use single point excitation, e.g. a bonded piezoelectric actuator [3, 4], a non-contact air-coupled piezoelectric actuator [5, 6] or a pulsed laser [7], combined with scanning laser Doppler vibrometer (SLDV) measurements. Due to reciprocity in the linear domain, one could also use scanning pulsed laser excitation combined with single point piezoelectric or laser Doppler vibrometer measurements [7, 8]. As an example, Sohn et al. [9] used pulsed laser excitation in combination with laser Doppler vibrometer measurements to achieve non-contact detection of fatigue cracks. The experimental approaches provide a 3D dataset of the velocity of vibration at each point of the component in function of time.

In the last decades, multiple methods were developed to convert the full wavefield dataset to a damage map [10-22]. For the method to be successful, the obtained damage map must reveal all defects and preferably also allow for defect evaluation (i.e. estimate the size and/or the depth). Among others, local wavenumber estimation (LWE) has gained a lot of attention as it seems promising for accurate defect detection and quantification. As the name indicates, the wavenumber of a specific Lamb mode is estimated at each point of the component. For simplicity, the working principle of local wavenumber estimation is now explained for linear isotropic materials. For linear isotropic materials, the Rayleigh-Lamb equation (also referred to as the dispersion relation) [2] gives the relation between the local wavenumber *k* [1/m], the temporal frequency of the wave *f* [Hz] and the local material thickness *d* [m]:

$$\frac{\tanh\left(\frac{\beta d}{2}\right)}{\tanh\left(\frac{\alpha d}{2}\right)} = \left[\frac{\left((2\pi k)^2+\beta^2\right)^2}{4\alpha\beta(2\pi k)^2}\right]^s \quad \text{with} \quad \begin{matrix} \alpha^2 = (2\pi)^2\left(k^2 - \frac{f^2}{c_l^2}\right) \\ \beta^2 = (2\pi)^2\left(k^2 - \frac{f^2}{c_t^2}\right) \end{matrix} \tag{1}$$

Where c_l and c_t are the material's longitudinal and transverse wave velocity, respectively. The parameter *s* equals +1 or -1 for the anti-symmetric or symmetric Lamb modes, respectively. The equation has to be solved numerically and the solutions are the dispersion curves of the material. In the case of anisotropic materials, for instance composites, no analytical expression such as Eq. (1) can be found (without approximations) and the dispersion curves need to be derived using numerical tools. As an example, the dispersion curves of (isotropic) aluminum (c_l = 6420 m/s, c_t = 3040 m/s) are shown in Figure 1. In Figure 1 (a), the solution is given in terms of the wavenumber-thickness product versus the frequency-thickness product, resulting in a single dispersion curve that is valid for any material thickness *d*. In Figure 1 (b), the dispersion curves are shown for an aluminum plate of specified thicknesses. Note that for the A_0 mode, the wavenumber increases when the material thickness becomes smaller. As such, a horizontal crack in the aluminum plate will result in the local increase of the A_0 mode wavenumber as graphically illustrated on Figure 1 (c). In the same way, a delamination defect in a composite plate results in an increased local wavenumber for the A_0 mode.

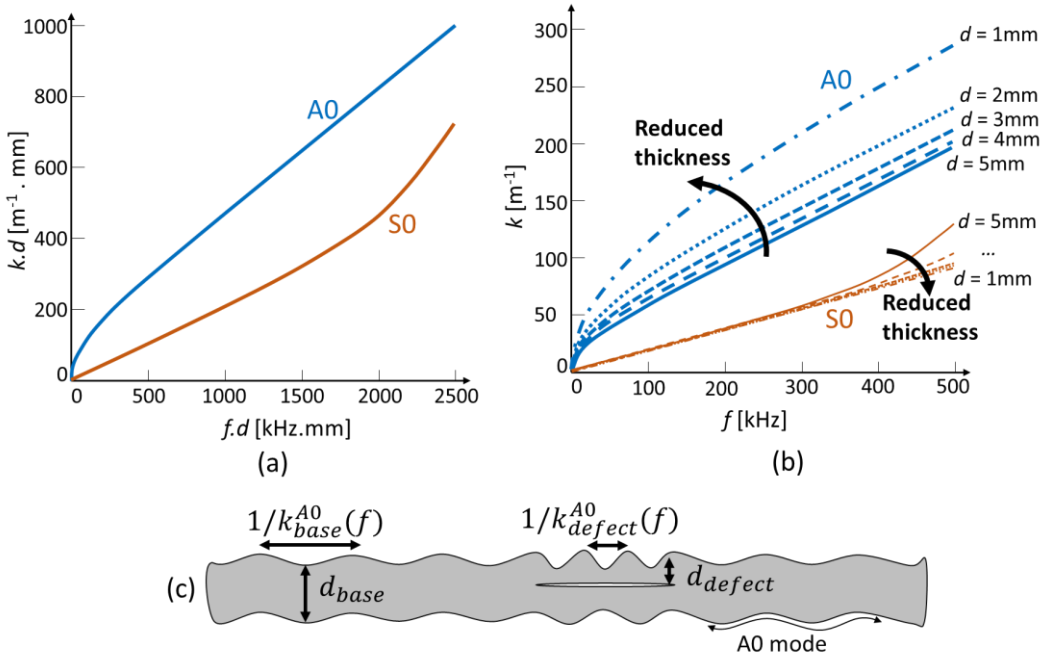

Figure 1: Dispersion characteristics of aluminum material: (a) Dispersion curves expressed as wavenumber-thickness *k.d* in function of frequency-thickness *f.d*, (b) Dispersion curves expressed as wavenumber *k* in function of frequency *f* for several material thicknesses *d* and (c) Schematic illustration of the local change in A_0 mode dispersion behavior at a horizontal crack or delamination.

Multiple LWE algorithms were developed, also resulting in a multitude of other names for LWE such as, acoustic wavenumber spectroscopy, instantaneous wavenumber estimation, multi-frequency LWE, etc. A distinction can be made based on the type of input data. Originally, LWE was developed for finding the local wavenumber map corresponding to a narrowband toneburst response with specific center frequency f_c [23, 24]. This toneburst response can be obtained using (i) piezoelectric excitation with a Hanning windowed sine voltage signal [24], (ii) piezoelectric excitation with a deterministic broadband voltage signal followed by a frequency filtering procedure [25] or (iii) pulsed laser excitation followed by a narrowband frequency bandpass filter [23]. In addition, LWE can be performed for standing wave excitation (i.e. steady-state regime) [26, 27] or using a single time or frequency frame (i.e. instantaneous LWE) [28].

All the mentioned LWE approaches have in common that the wavenumber map is obtained corresponding to a specific (center) frequency of excitation and a specific Lamb mode. In most cases the A_0 mode is chosen because the A_0 mode dispersion curve varies in function of the material's thickness *d* over the complete frequency axis (see Figure 1 (b)). For the S_0 mode, the dispersion curve only starts to become thickness-dependent for frequencies higher than 400 kHz (in case of a 5 mm thick aluminum plate). Excitation and measurement of these high frequency vibrations is difficult, which favors the A_0 mode to be used for LWE instead of the S_0 mode. Note however that the depth sensitivity of the A_0 mode decreases considerably when the material thickness becomes higher. As such, the use of the S_0 mode in combination with high frequency excitation can be required for detection of deep defects in thick materials (see also [29]).

Multiple researchers investigated the effect of the excitation (center) frequency on the obtained local wavenumber map [29-32]. It was concluded that the optimal excitation frequency depends on (i) the Lamb mode of interest, (ii) the dispersion characteristics (i.e. the material properties), (iii) the size and depth of the defect and (iv) the frequency-dependent signal-to-noise ratio (SNR) of the experimental setup. In addition to the optimal excitation frequency, also the optimal value of many LWE algorithm's parameters (e.g. the spatial window size used in the LWE approach based on the short-time-Fourier transform [24]) depends on the above listed characteristics. Hence, selection of this optimal excitation

frequency and the algorithm's parameters is far from straightforward in a realistic test case with material properties and unknown defect characteristics.
From the estimated local wavenumber map, the local thickness of the material can then be derived if the dispersion relations, and thus the material's elastic properties, are a priori known [8, 28-30]. Especially for composite materials with multiple plies and anisotropic stiffness parameters, this could become problematic.

In this study, a novel LWE approach is proposed by considering broadband excitation and subsequent self-reference mode filtering in the wavenumber-frequency domain. The broadband response of the test specimen is obtained using sine sweep piezoelectric excitation or pulsed laser excitation, combined with SLDV measurements. The novel self-reference broadband local wavenumber estimation (SRB-LWE) approach aims to:

- Overcome the problem related to the selection of an optimal excitation frequency.
- Improve the obtained damage map by using an enhanced filtering procedure.
- Avoid the need for manual parameter optimization.
- Obtain an estimated local thickness map (rather than a local wavenumber map) without the need for the material's stiffness properties, layup and density.

The only parameter that needs to be known in advance is the base material thickness (or most prominent thickness) of the investigated test specimen. And even in case that also this thickness is unknown, the SRB-LWE will give the relative local thickness compared to the base material (put as 1 mm).

First, the measurement procedure and the used test specimens are described. Next, the novel SRB-LWE algorithm is demonstrated on the measurement data of an aluminum plate with various flat bottom hole defects. Afterwards, the defect detection and depth identification capability of SRB-LWE is evaluated for two stiffened CFRP aircraft panels: (i) a 1.5 mm thick panel with a disbond at a backside stiffener and (ii) a 4 mm thick panel that suffered three low velocity impacts at different impact energies.

2. Materials and Measurements

SRB-LWE is performed on five different test specimens (see Figure 2).
The first three test specimens are 400x400x5 mm^3 aluminum plates. Ten flat bottom holes (FBHs) with specified diameter (Ø 15 mm, Ø 25 mm and Ø 35 mm, respectively) are milled into the backside of each plate. Figure 2 (a) shows the plate with FBHs of diameter 25 mm together with a table wherein the remaining material thickness *d* and the diameter Ø of every FBH are specified. Note that there are three FBHs with a remaining thickness of 0 mm that are thus open holes.
The fourth and fifth component are CFRP parts manufactured for use in the vertical stabilizer of an Airbus A320 aircraft. On the backside, stiffeners are visible which are bonded to a base plate. The thickness of the base plate, on which the stiffeners are bonded, measures 1.5 mm and 4 mm, respectively for the fourth and fifth component. The components are manufactured using a cross-ply layup. The material's elastic properties and densities are unknown. The component shown in Figure 2 (b) was scrapped by the manufacturer because an ultrasonic C-scan inspection revealed a defect at the central stiffener. The component shown in Figure 2 (c) suffered impacts at three locations with a 7.1 kg weight from a height of 20 cm, 35 cm and 30 cm. The corresponding theoretical impact energy equals 14 J, 24 J and 21 J, respectively. These three impact events resulted in three areas of barely visible impact damage (BVID) marked as BVID-A, BVID-B and BVID-C, respectively. Also shown in Figure 2 (b-c) are the time-of-flight (TOF) and relative amplitude (Amp) images obtained from in-house immersion ultrasonic C-scan inspection using a 5 MHz focused transducer in reflection mode. The C-scan results in Figure 2 (b) reveal a relatively large disbond between the central stiffener and the base plate. The C-scans of BVID-B reveal a complex distribution of delaminations and cracks (see Figure 2 (c)).

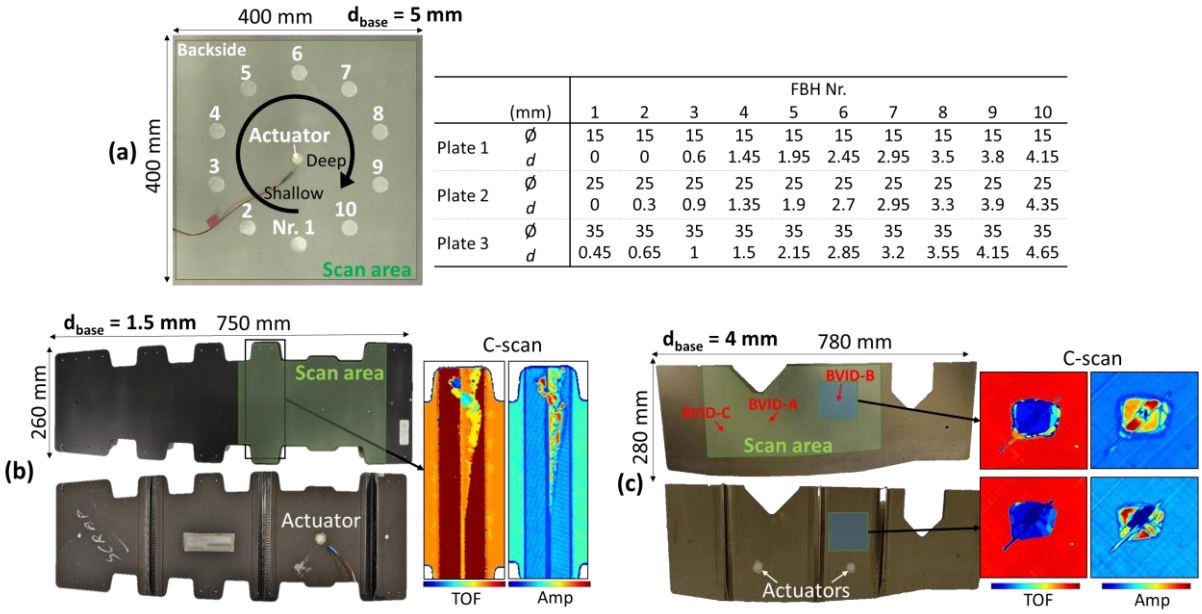

	(mm)	FBH Nr. 1	2	3	4	5	6	7	8	9	10
Plate 1	Ø	15	15	15	15	15	15	15	15	15	15
	d	0	0	0.6	1.45	1.95	2.45	2.95	3.5	3.8	4.15
Plate 2	Ø	25	25	25	25	25	25	25	25	25	25
	d	0	0.3	0.9	1.35	1.9	2.7	2.95	3.3	3.9	4.35
Plate 3	Ø	35	35	35	35	35	35	35	35	35	35
	d	0.45	0.65	1	1.5	2.15	2.85	3.2	3.55	4.15	4.65

Figure 2: Test specimen: (a) Three aluminum plates with each 10 flat bottom holes of specified diameter Ø (= 15, 25 and 35 mm, respectively) and remaining material thickness *d,* (b) CFRP aircraft panel with disbond at the central stiffener ($CFRP_{DISB}$) and (c) CFRP aircraft panel impacted at three locations ($CFRP_{BVID}$).

In each component, vibrations are introduced through small, low power piezoelectric actuators (Ekulit type EPZ-20MS64W). The actuators are attached to the backside using phenyl salicylate which has the advantage that the actuators can be easily removed by re-melting (> 41 °C) this bonding substance. A broadband sine sweep voltage signal is generated using the SLDV's built-in function generator. The sweep's start and end frequencies are listed in Table 1. The voltage signal is amplified through a Falco WMA-300 high voltage amplifier before it is supplied to the piezoelectric actuator. For the CFRP aircraft panel with BVID, two piezoelectric actuators are used. The actuators are located at the backside of the component in between the stiffeners (see Figure 2 (c)). The use of multiple actuators makes sure that the guided waves, which are partially reflected at the stiffeners, are of sufficient amplitude throughout the scan area.

As an alternative to the contact piezoelectric actuator, the aluminum plate with FBHs of diameter 35 mm has also been excited by a pulsed laser. A compact diode pumped solid state laser (Quantel VIRON) with wavelength 1064 nm, pulse duration < 12 ns, beam diameter 3.8 mm, repetition rate 20 Hz and maximum pulse energy 50 mJ is positioned behind the component (distance ≈ 1.5 m, angle ≈ 30°). Laser pulses are fired to the center of the aluminum plate. Elastic waves are formed due to the thermo-elastic effect induced by the laser pulses [7] resulting in a non-contact excitation method.

Table 1: Characteristics of excitation signals and SLDV data acquisition.

Material	Defect	Excitation			SLDV				
		f_{start} (kHz)	f_{end} (kHz)	Vpp	f_s (kS/s)	# samples	# averages	point spacing (mm)	Scan time (min)
Al 5 mm	FBH Ø 15 mm	5	300	50	625	10 000	20	3	88
	FBH Ø 25 mm	5	300	100	1250	10 000	20	3	46
	FBH Ø 35 mm	5	300	100	625	10 000	10	3	48
	FBH Ø 35 mm	Pulsed laser			625	2 500	10	3	114
$CFRP_{DISB}$	Disbond	20	250	100	1250	10 000	20	1.6	115
$CFRP_{BVID}$	3 x BVID	5	250	50	625	10 000	15	2	108
	BVID-B Front	5	300	100	625	10 000	10	1	35
	BVID-B Back	5	300	100	625	10 000	10	1	35

The full wavefield velocity response is recorded using a 3D infrared SLDV (Polytec PSV-500 3D Xtra). The area for which the wavefield is recorded (i.e. scan area) is indicated on Figure 2 for each test specimen. For the impacted CFRP panel (Figure 2 (c)), two additional measurements are performed focusing only on the BVID-B area. All relevant data acquisition settings, i.e. sampling frequency f_s, number of samples, number of averages and scan point spacing are included in Table 1. Also included in Table 1 is the total scan time. For this study, the SLDV settings were not optimized for low scan times. For the pulsed laser, the repetition rate was limited to 20 Hz. As a result, the inspection times are relatively long. Current research of the authors (and of multiple other research groups) focusses on methods for reducing the inspection time considerably. As an example, current authors introduced out-of-sight nonlinear local wave-direction estimation as a fast initial inspection tool [33]. In addition, different research groups showed that the compressive sensing algorithm can be used to reconstruct the full wavefield response out of a limited amount of distributed measurement points [15, 34-36]. Reduction of the inspection time is also achieved through steady-state LWE [26, 27]. Although note that the proposed SRB-LWE approach has specific advantages over the traditional steady-state or toneburst LWE method (see Section 3.4). At last, Li et al. [37] developed a six beam LDV based on silicon photonics technology. Their findings illustrate that it is possible to construct affordable LDV systems with large amount of beams, therefore reducing the measurement time.

In this study, the out-of-plane velocity component $V_Z(x, y, t)$ is used because the SRB-LWE algorithm is operated on the A_0 Lamb mode (see further), which has a dominant out-of-plane surface vibration. Figure 3 shows time snapshots of the measured out-of-plane velocity component for the different test specimens. From these snapshots, it is impossible to identify most of the defects, illustrating the need for advanced signal processing.

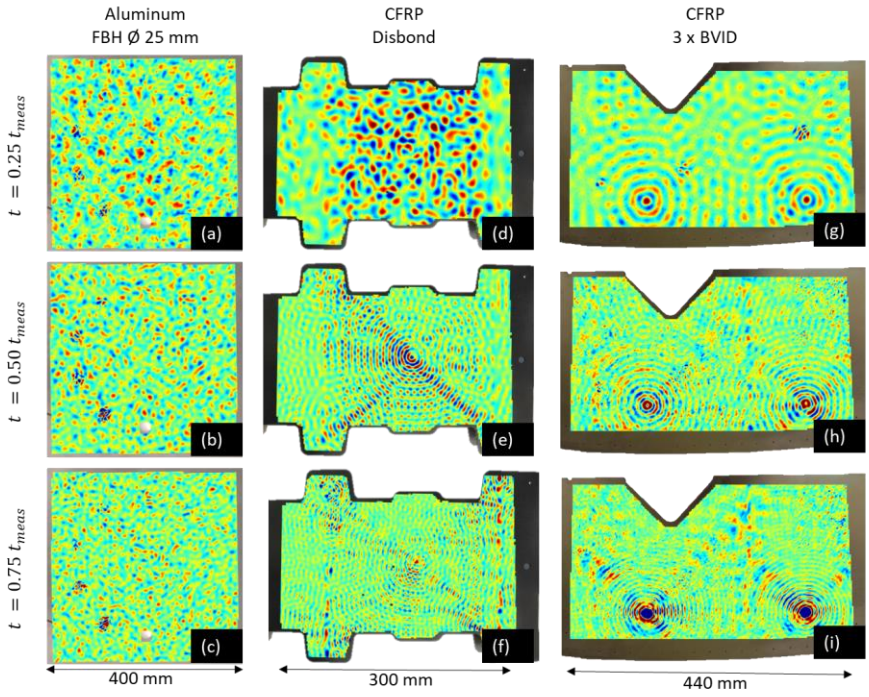

Figure 3: Time snapshots of the out-of-plane velocity of vibration: (a-c) Aluminum plate with 25 mm FBHs, (d-f) CFRP aircraft panel with disbond at stiffener and (g-i) CFRP aircraft panel with BVIDs.

3. Self-reference Broadband LWE Algorithm

The SRB-LWE algorithm consists of multiple signal processing steps that are discussed in detail in the following subsections. The measurement dataset of the aluminum plate with FBHs of diameter 25 mm is used throughout this section. As an additional aid in understanding the SRB-LWE procedure, a flow chart is provided in which all separate steps, and a selection of intermediate results, are shown (see Figure 4).

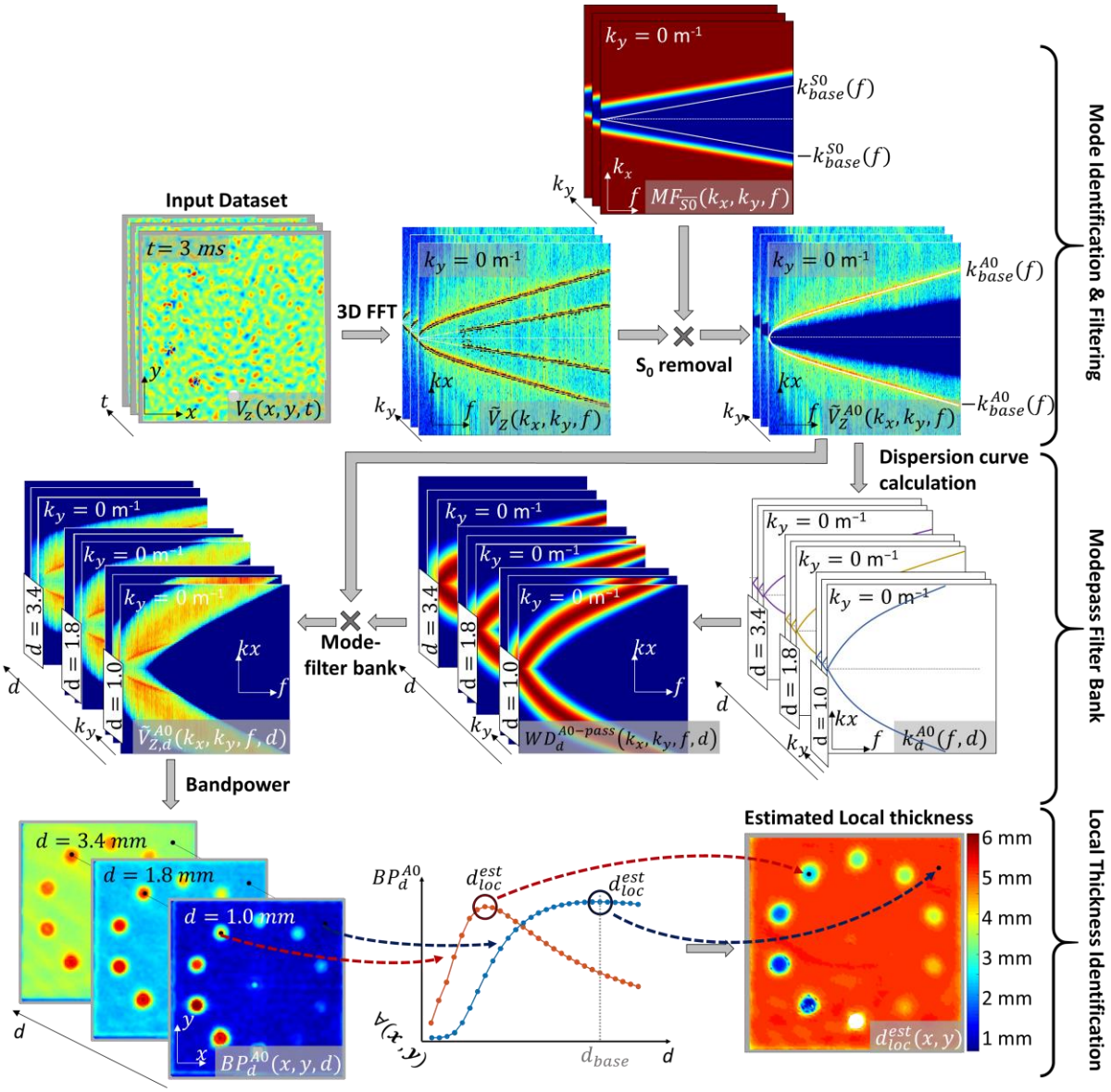

Figure 4: Flow chart of the self-reference broadband local wavenumber estimation algorithm.

3.1. Mode Identification and Filtering

The SRB-LWE procedure is performed for one Lamb mode of interest. As a result, if other modes of significant amplitude are present, they have to be removed from the dataset through a filtering procedure in the wavenumber-frequency domain [13, 38]. Note that this step is likewise performed in the traditional narrowband LWE algorithms. This mode identification and removal step corresponds to the first row in the flow chart provided in Figure 4.

3.1.1. Dispersion Curve Identification.

Assuming unknown material properties, the dispersion curves must first be identified from the broadband measurement result. The recorded dataset $V_Z(x,y,t)$ is transformed from the spatial-time domain (x,y,t) to the wavenumber-frequency domain (k_x,k_y,f) using 3D fast Fourier transformation. Figure 5 (a) shows a 3D representation of the obtained dispersion map. The dispersion curves of the A_0 and S_0 Lamb modes are visible as lines of increased intensity. It is assumed that the area of the defected material is significantly smaller compared to the area of the damage-free base material. Under this assumption, the dispersion curves seen in Figure 5 (a) correspond in good approximation to the damage-free base material.

Multiple methods can be used to identify the dispersion curves in an automated manner e.g. the matrix-pencil algorithm [39], inhomogeneous wave correlation (IWC) [40] or an iterative curve detection procedure in the wavenumber-frequency domain [23]. As an example, Figure 5 (b) shows the mode curves, $k_{base}^{A0}(f)$ and $k_{base}^{S0}(f)$ (along k_y = 0), which were identified using the iterative curve detection procedure outlined in Ref. [23].

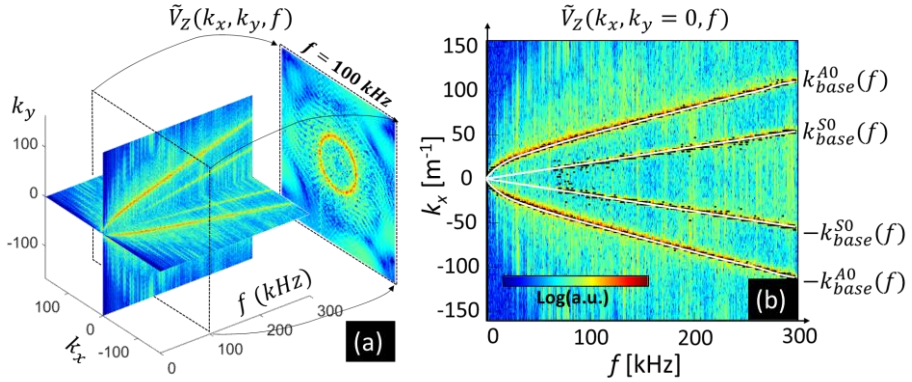

Figure 5: Out-of-plane velocity response of the aluminum plate with Ø 25 mm FBHs (a) 3D wavenumber-frequency map, (b) Wavenumber-frequency map along k_y = 0, together with the identified dispersion curves of the A_0 and S_0 Lamb modes.

In this study, the A_0 mode is chosen as the mode of interest on which the SRB-LWE algorithm is applied. This is motivated by the high depth sensitivity of the A_0 mode in the excited frequency range (see also Figure 1 (b)). In addition, the A_0 mode is less affected by the potential anisotropic nature of the test specimen (compared to the S_0 mode), which simplifies the design of the filter bank in wavenumber-frequency domain. A discussion about the effect of anisotropy on the proposed SRB-LWE method is provided in Section 3.2.2.

3.1.2. S_0 Mode Removal

The vibrations corresponding to the S_0 mode are removed from the dataset using a frequency-dependent bandstop filter in the wavenumber-frequency domain. The bandstop filter WD_{stop}^{S0} is constructed around the previously identified S_0 dispersion curve $k_{base}^{S0}(f)$:

$$WD_{stop}^{S0}(\mathrm{k_x}, \mathrm{k_y}, \mathrm{f}) = \begin{cases} 0 & \text{if } D(\mathrm{k_r}, \mathrm{f}) \leq FT \\ \frac{1}{2} - \frac{1}{2}\cos\left(\frac{4\,(|D(\mathrm{k_r}, \mathrm{f})| - FT)}{BW_{S0}}\right) & \text{if } FT < D(\mathrm{k_r}, \mathrm{f}) < FT + \frac{\pi}{4}BW_{S0} \\ 1 & \text{if } D(\mathrm{k_r}, \mathrm{f}) \geq FT + \frac{\pi}{4}BW_{S0} \end{cases} \quad (2)$$

$$\text{with} \quad k_r = \sqrt{k_x^2 + k_y^2}$$

$$D(\mathrm{k_r}, \mathrm{f}) = k_r - k_{base}^{S0}(f)$$

where FT is the flat top length and BW_{S0} is the half power bandwidth of the cosine lobe. The following filter parameters are used FT = 5 m^{-1} and BW_{S0} = 10 m^{-1} which leads to the removal of the vibrations related to the S_0 mode, as well as the removal of the noise associated with very low wavenumbers. These filter parameter values are also applicable for other materials or other base material thicknesses. The filter is shown in Figure 6 (a).

The required A_0 mode response is obtained after multiplication of the mode-removal filter WD_{stop}^{S0} with the out-of-plane velocity response $\tilde{V}_Z$ in the wavenumber-frequency domain (see Figure 6 (b)):

$$\tilde{V}_Z^{A0}(k_x, k_y, f) = WD_{stop}^{S0}(k_x, k_y, f).\tilde{V}_Z(k_x, k_y, f) \quad (3)$$

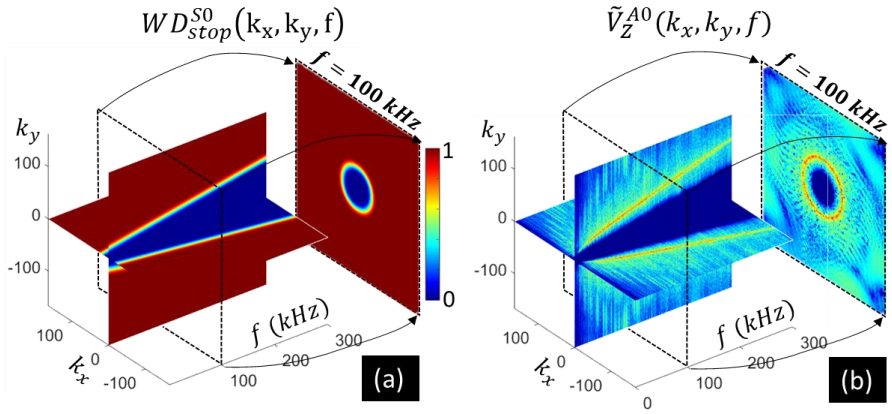

Figure 6: 3D view of (a) S_0 Lamb mode removal filter and (b) wavenumber-frequency map for the out-of-plane velocity response after applying the S_0 mode removal filter.

Note that it is also possible to obtain the required A_0 mode response $\tilde{V}_Z^{A0}(k_x, k_y, f)$ using a bandpass filter constructed around the A_0 mode curve (instead of a bandstop filter around the S_0 mode curve). However, the authors advise against this approach because the selection of the bandpass filter's bandwidth would become critical. If the A_0 bandpass filter's bandwidth is set too low, the filter would partially remove vibrations at the defects, resulting in an inferior estimated local thickness map and potentially even missing the deep defects. On the other hand, if the bandwidth is set too high, the filter can allow vibrations of the S_0 mode to pass, which would also result in an inferior estimated local thickness map.

3.2. Mode Filter Bank

The next big step in the SRB-LWE algorithm is the construction and application of a mode filter bank (see second row in the flow chart of Figure 4).

3.2.1. Construction of the Mode Filter Bank

The dispersion curve of the mode of interest (i.e. $[f, k_{base}^{A0}]$, as identified in Section 3.1) corresponds to the dispersion behavior of the damage-free base material with thickness $d = d_{base}$. The dispersion curves corresponding to the same material but with a different thickness *d* are derived from $[f, k_{base}^{A0}]$ using a scaling procedure along both the frequency and the wavenumber axis:

$$[f, k_{base}^{A0}] \overset{d}{\Rightarrow} \left[\frac{f \,.\, d_{base}}{d}, \frac{k_{base}^{A0} \,.\, d_{base}}{d}\right] \Rightarrow [f, k_d^{A0}] \tag{4}$$

This derivation is based on the thickness invariance of the dispersion curves when plotted on a $k.d$ versus $f.d$ coordinate system (see also Figure 1 (a)). The assumptions connected to the use of Eq. (4) are discussed in Section 3.2.2. For the aluminum plate with FBHs, the dispersion curves are calculated for assumed material thicknesses *d* = 0.2 mm, 0.4 mm … 6 mm. Figure 7 (a) shows the obtained dispersion curve for the A_0 mode in aluminum (thickness *d* = 3 mm) derived from $[f, k_{base}^{A0}]$ using Eq. (4). In addition, the theoretical dispersion curve is included that is calculated using Eq. (1) with material properties obtained from the manufacturer (i.e. Lamé constants: λ = 56.4 GPa, μ = 26.15 GPa and density ρ = 2693 kg/m^3). Excellent agreement between both curves is observed, confirming the proposed self-reference approach. Figure 7 (b) shows a selection of the obtained dispersion curves for various thicknesses. Note again that the wavenumber increases when the thickness *d* is reduced and that the distance between the different dispersion curves becomes smaller for higher material thicknesses.

A cosine shaped bandpass filter is constructed around each thickness-specific dispersion curve k_d^{A0}:

$$WD_d^{A0-pass}(k_x,k_y,f,d)=\begin{cases}0 & \text{if } D(k_r,f,d)>\dfrac{BW_{A0}(f)}{2}\\ \dfrac{1}{2}+\dfrac{1}{2}\cos\left(\dfrac{2\pi\, D(k_r,f,d)}{BW_{A0}(f)}\right) & \text{elsewhere}\end{cases} \tag{5}$$

$$\text{with}\quad k_r=\sqrt{k_x^2+k_y^2}$$
$$D(k_r,f,d)=\left|k_r-k_{\mathrm{d}}^{A0}(f,d)\right|$$

The bandwidth $BW_{A0}(f)$ of the bandpass filter is function of the frequency and is defined as:

$$BW_{A0}(f)=k_{max}-k_{\mathrm{base}}^{A0}(f)\qquad \text{with}\quad k_{max}=\frac{1}{2\,\Delta x} \tag{6}$$

where k_{max} is the maximal observable wavenumber for a measurement with equidistant scan point spacing $\Delta x=\Delta y$. This definition of $BW_{A0}(f)$ makes optimal use of the available information in the wavenumber domain, and avoids manual selection. As an example, Figure 7 (c) and (d) show the bandpass filter corresponding to a material thickness *d* = 1.8 mm. Note that it should be avoided to vary the bandwidth BW_{A0} directly in function of the material thickness *d*, because this would imply that every $WD_d^{A0-pass}$ filter passes a different amount of energy (and noise).

The A_0 mode velocity response $\tilde{V}_Z^{A0}(k_x,k_y,f)$ is passed through this dispersion curve filter bank:

$$\tilde{V}_{Z,d}^{A0}(k_x,k_y,f,d)=WD_d^{A0-pass}(k_x,k_y,f,d).\tilde{V}_Z^{A0}(k_x,k_y,f) \tag{7}$$

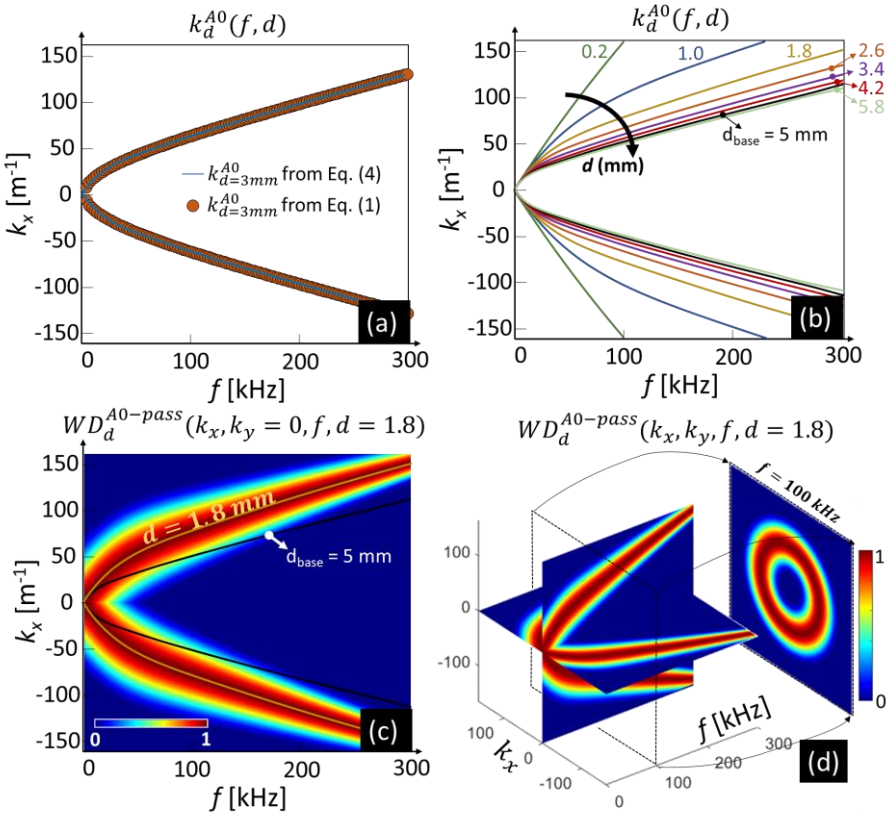

Figure 7: (a) A_0 mode curves for 3 mm thick aluminum calculated using Eq. (4) and using Eq. (1), (b) A_0 mode curves of different material thickness *d* for the aluminum plate with Ø 25 mm FBHs and (c-d) 2D and 3D representation of the mode bandpass filter constructed around the dispersion curve corresponding to material thickness *d* = 1.8 mm.

3.2.2. Assumptions

Two important assumptions are associated with the use of equations (4) to (7).

First, the derivation of the dispersion curves for different material thicknesses (Eq. (4)) is strictly speaking only valid for materials of which the stiffness tensor is constant throughout the thickness. However, layered composite components have ply-dependent elastic properties, resulting in locally different homogenized stiffness in the presence of a delamination.
Second, the mode bandpass filters (see Eq. (5)) are circular cone-shaped in the (k_x, k_y, f) domain (see Figure 7 (d)) and thus do not take into account potential strong anisotropy of the medium. Note that this assumption is also made in the traditional implementations of LWE (which use wavenumber filters). While the effect of anisotropy on the A_0 mode dispersion behavior is limited for quasi-isotropic and cross-ply CFRPs (as considered in this study), it can result in a less accurate defect evaluation in the case of unidirectional composites.

In case all material properties (density, ply thickness, ply stiffness tensor, layup) are known, it is possible to relax both assumptions. In that case, the dispersion curves can be calculated for a delamination at every possible ply interface (instead of using Eq. (4)) and along every specific propagation direction $\theta = \arctan\left(\frac{k_y}{k_x}\right)$. Using these angular- and depth-dependent dispersion curves $k_d^{A0}(\theta, f)$, the mode bandpass filters derived using Eq. (5) become non-circular cone-shaped (e.g. elliptical cone-shaped). A recent study [ref] investigated such a local wavenumber to local depth conversion for a quasi-isotropic CFRP.

In practice however, the ply thickness, ply stiffness and layup of the evaluated CFRPs are often unknown. If one would consider the full wavenumber-frequency map of the measured velocity response, it will provide knowledge on the global dispersion behavior of the base material. However, it cannot provide information on the local dispersion behavior in the presence of a delamination. As a result, Eq. (4) and the associated assumptions cannot be relaxed without having complete knowledge on the ply parameters and layup of the composite.
The depth estimation in this study is obtained through the proposed SRB-LWE for CFRPs parts for which no prior knowledge on material properties was available. Hence, the above two assumptions might result in small discrepancies in the estimated local thickness maps derived for the layered cross-ply composite components. This is further discussed in Section 4.2 (inspection of two cross-ply CRFP aircraft panels) where it is shown that although there are small discrepancies observed, they do not adversely affect the defect assessment.

3.3. Local Thickness Identification

As a last step, the local thickness map is constructed. The workflow can be found in the last row of Figure 4.

In order to estimate the local thickness, the 4D dataset $\tilde{V}_{Z,d}^{A0}(k_x, k_y, f, d)$ is transformed back to the spatial domain using the inverse FFT along the k_x, k_y dimensions. The obtained dataset $V_{Z,d}^{A0}(x, y, f, d)$ represents the out-of-plane velocity at location (x, y) associated to a specific material thickness d and excitation frequency f. Its local bandpower density is derived as:

$$BP_d^{A0}(x, y, d) = \frac{1}{\sum_{f=0}^{f_{max}(d)}(TH(f))} \sum_{f=0}^{f_{max}(d)} \left(\frac{\left|V_{Z,d}^{A0}(x,y,f,d)\right|^2}{WF(f)} TH(f) \right) \qquad \text{unit}\left[\left(\frac{m}{s}\right)^2 / Hz\right] \quad (8)$$

The calculation of the bandpower using Eq. (8) requires the prior calculation of the weighting factors $WF(f)$ and the threshold mask $TH(f)$.

The dimensionless frequency-dependent weighting factor $WF(f)$ compensates for the fact that the excitation source does not excite all frequency bins with the same amount of energy [4]. They are defined as:

$$WF(f) = \frac{\sum_{(x,y)} \left| V_{Z,d}^{A0}(x,y,f,d_{base}) \right|^2}{\sum_{(x,y,f)} \left| V_{Z,d}^{A0}(x,y,f,d_{base}) \right|^2} \tag{9}$$

The numerator represents the energy of vibration in the base material summed over all scan points and the denominator makes the weighting factor dimensionless.

At some frequencies, the excited wavefield is of low amplitude resulting in a low signal-to-noise ratio (SNR). This is often the case in the high frequency regime where the wave damping is high, the piezoelectric actuators are less effective and the intrinsic noise level of the SLDV increases. The threshold function $TH(f)$ is used to avoid that these frequency frames, with low SNR, are not taken into account in the calculation of the bandpower density. In case of a deterministic sine sweep excitation, the SNR can be derived as:

$$SNR(f) = \frac{E(f)}{E\left(0.5 f_{min}^{actuator}\right) + \frac{f - f_{min}^{actuator}}{f_{max}^{actuator} - f_{min}^{actuator}} \left[E\left(1.25 f_{min}^{actuator}\right) - E\left(0.5 f_{max}^{actuator}\right) \right]} \tag{10}$$
$$\text{with } E(f) = \sum_{(x,y)} |V_Z(x,y,f)|^2$$

The frequency-dependent noise level (i.e. the denominator) is based on the observed amplitude of the out-of-plane velocity signal at frequencies below the minimum excited frequency ($f_{min}^{actuator}$) and above the maximum excited frequency ($f_{max}^{actuator}$). The corresponding threshold value SNR_{Thres} and threshold mask $TH(f)$ are defined as:

$$SNR_{Thres} = \frac{0.95}{f_{max}^{actuator} - f_{min}^{actuator}} \sum_{f=f_{min}^{actuator}}^{f_{max}^{actuator}} SNR(f) \tag{11}$$
$$\text{and} \quad TH(f) = \begin{cases} 0 & \text{if } SNR(f) < SNR_{Thres} \\ 1 & \text{elsewhere} \end{cases}$$

As an example, Figure 8 shows $SNR(f)$ for the aluminum plate with Ø 25 mm FBHs together with the threshold SNR_{Thres}. Due to the use of the SNR based threshold mask $TH(f)$, the minimum frequency used in the calculation of the bandpower (Eq. (8)) can simply be set at 0 Hz. This because the noisy frequency frames which are related to frequencies smaller than the minimum frequency of excitation are associated with a $TH(f)$ value equal to 0 (see Figure 8). As a result, these frequency frames are automatically disregarded in the calculation of the bandpower density. The frequency frames that are related to a frequency higher than the maximum frequency in the excitation signal are disregarded in similar manner (see Figure 8).

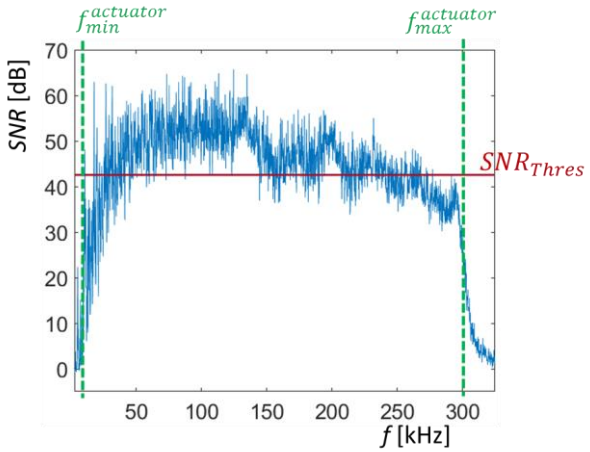

Figure 8: Signal-to-noise ratio for aluminum plate with Ø 25 mm FBHs with indication of the threshold used in the bandpower calculation.

Care has to be taken in the selection of the maximum frequency limit $f_{max}(d)$ used in Eq. (8). The maximum frequency $f_{max}(d)$ must be smaller than the frequency for which the thickness-specific dispersion curve reaches the maximum observable wavenumber: $k_{\mathrm{d}}^{A0}(f_{max}(d), d) = (2.GridSize)^{-1} = 167\ m^{-1}$. This criterion for $f_{max}(d)$ is illustrated in Figure 9 (see orange rectangle). Note that this criterion makes the maximum frequency of interest dependent on the evaluated thickness *d*. The maximum frequency of interest decreases for decreasing material thickness *d*.

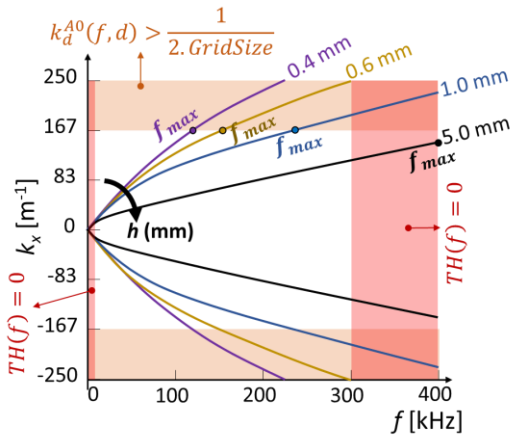

Figure 9: Illustration of the automated selection of the maximum frequency of interest for bandpower calculation in the aluminum plate with Ø 25 mm FBHs.

Figure 10 (a) shows the resulting $BP_d^{A0}(x, y, d)$ curve at three specific points corresponding to (i) a FBH with true remaining thickness 1.9 mm (p_1), (ii) a FBH with true remaining thickness 3.3 mm (p_2) and (iii) damage-free material with true thickness 5 mm (p_3). The local material thickness is estimated as thickness for which BP_d^{A0} becomes maximal:

$$d_{loc}^{est}(x, y) = \underset{d}{\mathrm{argmax}}\left[BP_d^{A0}(x, y, d)\right] \tag{12}$$

As seen on Figure 10 (a), the estimated local thickness d_{loc}^{est} closely corresponds to the true local thickness d_{loc}^{true}. Further note that the peak in the BP_d^{A0} curve becomes less pronounced for higher local thicknesses. This is the result of the decreasing distance between the k_{d}^{A0} curves for higher material thicknesses (see discussions of Figure 1 (b) and Figure 7 (a)). The estimated local thickness map $d_{loc}^{est}(x, y)$ is shown in Figure 10 (b). A more in-depth discussion of this map is provided in Section 4.1.

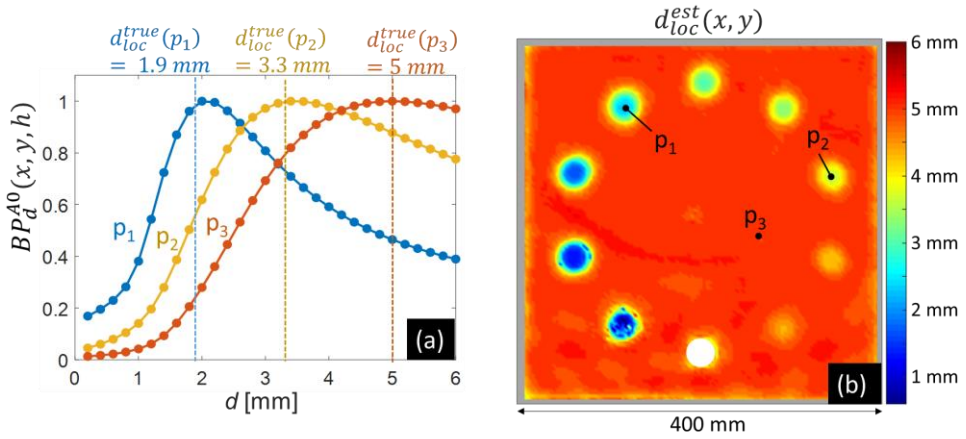

Figure 10: (a) Bandpower density in function of evaluated material thickness at three locations (p_1, p_2 and p_3) and (b) Estimated local thickness map for the aluminum plate with Ø 25 mm FBHs.

3.4. Advantages of SRB-LWE

The proposed SRB-LWE algorithm has some specific advantages over the traditional LWE approaches.

A first advantage is related to the use of a mode filter instead of a wavenumber filter. The mode filter ($WD_d^{A0-pass}$) follows the thickness-specific dispersion curve $k_d^{A0}(f)$. As a result, the central wavenumber of the mode filter is frequency-dependent. This is in contrast to the traditional LWE algorithms, in which wavenumber filters are used that are frequency-independent. The effect of both filter types is graphically explained in Figure 11 (a). Suppose that only the vibrations that correspond to a certain thickness of material must be extracted from the total burst response. The mode curve corresponding to this desired thickness is indicated in blue. When a mode filter (indicated in orange) is constructed around this curve, the vibrations are correctly filtered. On the other hand, in case a wavenumber filter (indicated in purple) is constructed around the central wavenumber, some vibrations are retained that correspond to a different material thickness (see dark gray color on inset). In addition, some of the vibrations that correspond to the desired thickness are removed (see light gray color on inset). Only when the input dataset would correspond to a steady-state sine response (i.e. an infinitely small bandwidth), a wavenumber filter is as effective as a mode filter. The current authors recently exploited this same mode filter concept for the calculation of a broadband mode-removed energy distribution in order to construct highly sensitive damage maps [13].

The second advantage of the proposed SRB-LWE is related to the estimation of the local thickness (or the local wavenumber) at a multitude of frequencies using a single experiment. This large number of evaluated frequencies results in an averaging effect that increases the robustness of LWE, especially when the SNR of the measurement is limited. This increase in robustness was also described by Juarez and Leckey [32] and Moon et al. [29] who performed the traditional LWE on multiple input datasets with varying center frequencies.

The broadband nature of the propose SRB-LWE also solves the problem of traditional LWE methods related to shallow defect detection. For traditional narrowband LWE, it proved impossible to detect shallow damages when using high center frequencies of excitation (see also later in Figure 11 (c)) [ref]. This because the maximum observable wavenumber k_{max} is lower than the true wavenumber at the shallow damage. For SRB-LWE, low and high frequencies are taken into account, resulting in a correct thickness estimation for shallow as well as deep defects.

The third benefit of the proposed algorithm is that the depth of the defect is readily obtained without the need to know material properties. Only the thickness of the base material d_{base} needs to be known for quantitative local thickness estimation. If d_{base} would be unknown, the procedure can still be used (by setting d_{base} = 1) and the estimated local thickness map will give the relative thickness compared to the base material.

At last, the parameters used in this self-reference broadband LWE implementation are defined in such a way that they are independent of the test case. In addition, the use of the threshold function $TH(f)$, based on the measurement's SNR, further diminishes the required user input and increases the robustness. This is in contrast to the traditional LWE techniques, which have several parameters that require manual tweaking when applied on measurements obtained for components with different base and defect thicknesses, different SNR, different scan point spacing or different expected defect types [23, 24, 32]. Thus, the proposed SRB-LWE largely improves the level of automation compared to the traditional LWE implementations.

As an example, the estimated local thickness map obtained using the SRB-LWE method (Figure 11 (b)) is compared with the estimated local thickness map obtained using the traditional LWE algorithm explained in [23] (Figure 11 (c)). The traditional LWE algorithm is operated on a 10-cycle Hanning windowed sine response with center frequency 200 kHz. This center frequency was selected by trial and error in order to improve the results. Also the bandwidth of the wavenumber filter was determined by trial and error for the given sample. The estimated local wavenumber map obtained through traditional LWE is converted into an estimated local thickness map using the wavenumber-thickness relations (at f = 200 kHz) derived with Eq. 4.
A line plot of the local thickness through two defects (Figure 11 (d)) is included to facilitate the comparison of the results. It can be seen that the estimated local thickness using the SRB-LWE technique is very good for the 5 mm thick base material (expect for a small area at the actuator), as well as for the 1.9 mm and 4.35 mm deep FBHs. The local thickness estimate obtained using the traditional LWE technique is less accurate as seen by the irregular curve plot. The difference in the quality of the estimated local thickness maps becomes even more pronounced for measurements with a lower SNR (see the results for the CFRP aircraft panel in Section 4.2.1).

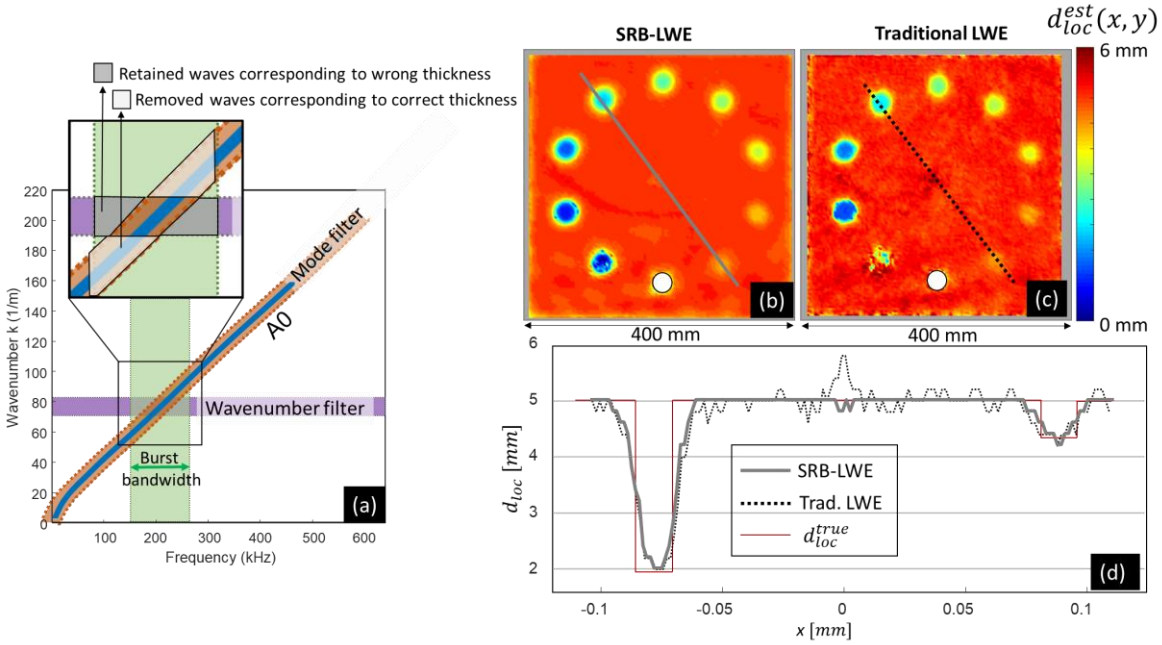

Figure 11: Comparison of the SRB-LWE technique using mode filters with the traditional LWE technique using wavenumber filters applied on the aluminum plate with Ø 25 mm FBHs: (a) Schematic illustration of both filter types, (b-c) Estimated local thickness map obtained using SRB-LWE (i.e. mode-filter) and traditional LWE (i.e. wavenumber filter), respectively, (c) Estimated local thickness along the line indicated on figures (b-c).

4. Results and Discussion

4.1. Aluminum Plates with FBHs

4.1.1. Piezoelectric Excitation

SRB-LWE is performed for the measurement results of three 5 mm thick aluminum plates that are excited using piezoelectric actuators, and which contain FBH defects of variable diameter and remaining material thickness (see also Figure 2 (a)). The resulting estimated local thickness maps are shown in Figure 12 (a-c). Figure 12 (d-f) show line plots of the estimated local thickness at the location of each FBH defect. The true defect diameter and the remaining thicknesses are indicated on these graphs using dashed lines. In addition, the estimated and true local thickness at the center of each FBH are listed in Table 2.

The estimated local thickness maps reveal all the FBH defects. In general, the estimated thickness is in good agreement with the true remaining material thickness as seen in Figure 12 (d-f) and in Table 2. Note that the thickness is estimated with a resolution of 0.2 mm. For the smallest FBHs (Ø 15 mm), the true local thickness is slightly underestimated. This is a known consequence of performing LWE with a limited maximum frequency of excitation and a limited scan point resolution (see also [29, 31]).
Figure 12 and Table 2 indicate that the SRB-LWE can be used successfully for the detection and evaluation of defects in isotropic materials in a fully automated manner. The estimated local thickness maps are of high quality and reveal all defects, including shallow defects as well as deep defects with a depth higher than 80% of the base material's thickness.

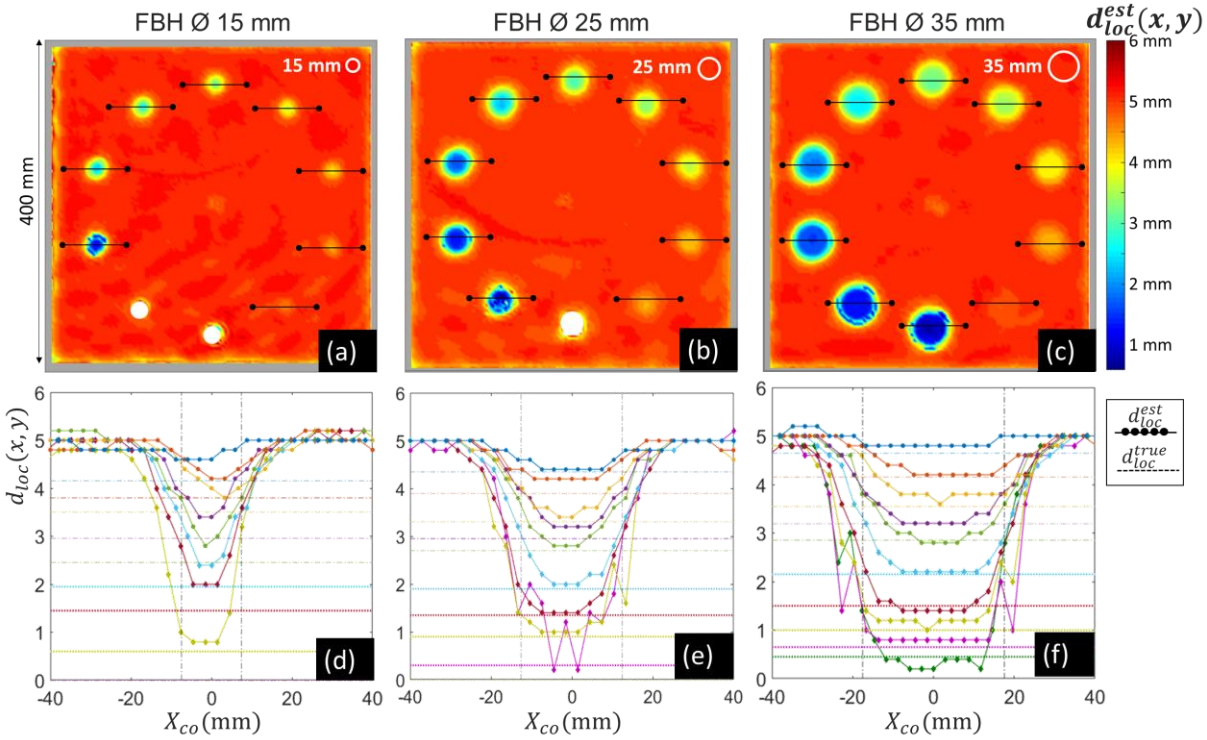

Figure 12: Results from the SRB-LWE, (a-c) Estimated local thickness maps and (d-f) Estimated local thickness at the FBHs for the three piezoelectric excited aluminum plates with FBHs of diameter 15, 25 and 35 mm, respectively.

4.1.2. Pulsed Laser Excitation

The proposed SRB-LWE algorithm can equally be used with pulsed laser excitation instead of piezoelectric excitation, resulting in a completely non-contact NDT approach. This is illustrated for the aluminum plate with FBH defects of diameter 35 mm.

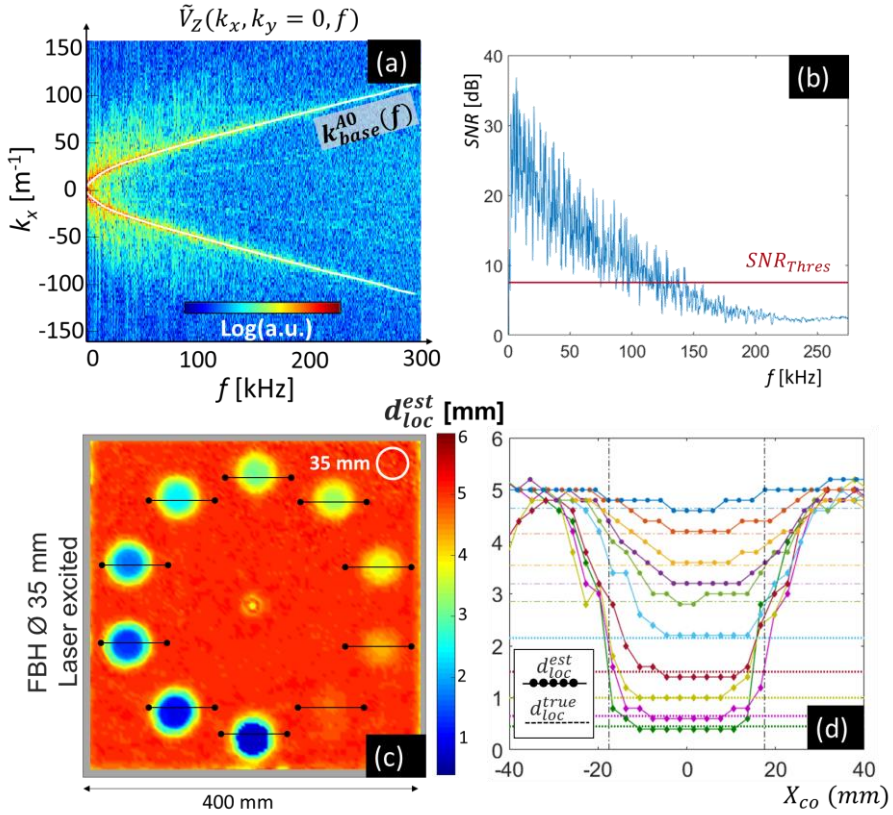

Figure 13 (a) shows the wavenumber-frequency map (along k_y = 0) for the out-of-plane velocity component excited by the pulsed laser. The SNR and the associated threshold value (see Eq. (11)) is shown in Figure 13 (b). Comparing this wavenumber-frequency map and SNR curve with the one corresponding to piezoelectric excitation (see Figure 5 and Figure 8, respectively) shows that (i) the pulsed laser excitation does not excite the S_0 mode efficiently and (ii) the amplitude of the laser excited A_0 mode decreases considerably for frequencies higher than 100 kHz. Therefore, frequencies in excess of ± 125 kHz are automatically disregarded (i.e. $TH(f > \pm 125) = 0$).

The resulting estimated local thickness map and the line plot of the estimated local thickness at each FBH defect is shown in Figure 13 (c-d), respectively. The estimated local thickness at each FBH has also been added to Table 2. It can be seen that a good correspondence is found between the true local thickness and the output of the SRB-LWE algorithm.

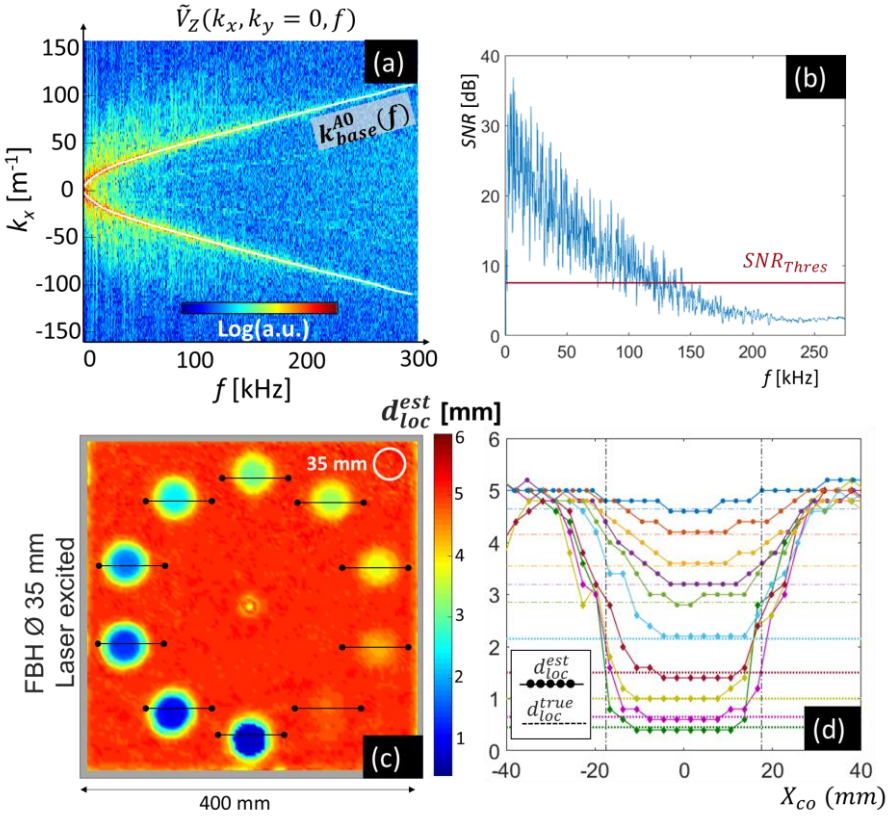

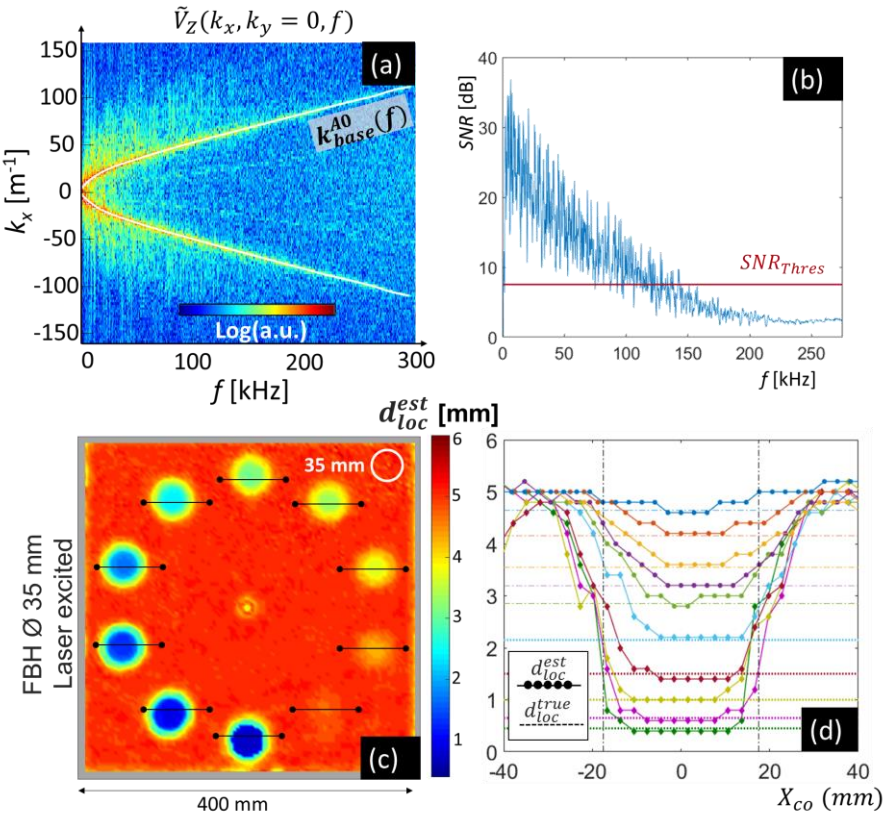

Figure 13: Laser excited aluminum plate with 35 mm FBHs (a) Wavenumber-frequency map for the out-of-plane velocity response along k_y = 0, (b) SNR with indication of the threshold, (c) SRB-LWE derived local thickness map and (c) Line plot of the estimated local thickness at FBHs.

Table 2: Estimated local thickness d_{loc}^{est} (mm) and true local thickness d_{loc}^{true} (mm) for each FBH in the three aluminum plates.

Ø (mm)	Nr.	1	2	3	4	5	6	7	8	9	10
15	d_{loc}^{true}	\	\	0.6	1.45	1.95	2.45	2.95	3.5	3.8	4.15
	$d_{loc}^{est-piezo}$	\	\	0.8	2	2.4	2.8	3.4	3.8	4.2	4.6
25	d_{loc}^{true}	\	0.3	0.9	1.35	1.9	2.7	2.95	3.3	3.9	4.35
	$d_{loc}^{est-piezo}$	\	0.2	1	1.4	2	2.8	3.2	3.4	4.2	4.2
35	d_{loc}^{true}	0.45	0.65	1	1.5	2.15	2.85	3.2	3.55	4.15	4.65
	$d_{loc}^{est-piezo}$	0.2	0.8	1	1.4	2.2	2.8	3.2	3.8	4.2	4.6
	$d_{loc}^{est-laser}$	0.4	0.6	1	1.4	2.2	3	3.2	3.6	4.2	4.6

4.2. Cross-ply CFRP A320 Aircraft Panels

SRB-LWE is performed on the measurement results of two stiffened cross-ply CFRP aircraft components (see also Figure 2 (b-c)). The thickness of the damage-free base material is respectively 1.5 and 4 mm. Note that the previously defined SRB-LWE's characteristics, for instance the bandwidth BW_{A0} in Eq. (6), are defined in such a way that they require no manual tweaking for new inspection cases.

4.2.1. Aircraft Panel with Disbond

The results of the 1.5 mm thick aircraft panel with a disbond at a stiffener are discussed first. The panel was manufactured by an industrial partner, and the disbond was unintentionally generated during the manufacturing process. The global wavenumber-frequency map (along k_y = 0 m^{-1}) of the measurement is displayed in Figure 14 (a), and the identified dispersion curves are shown on top with white lines. The evaluated thicknesses *d* range from 0.1 mm up to 3.9 mm in steps of 0.2 mm. In that way, it is possible to also estimate the increased thickness at the location of the backside stiffeners.

Figure 14 (b) shows the TOF map (converted to depth estimate) derived from the ultrasonic C-scan inspection. Except for the disbonded area, the local thickness at the stiffener equals 2.58 mm. Note that the thickness of the stiffener's middle fin (see also Figure 2 (b)) is not found using the time-of-flight C-scan results.

Figure 14 (c) and (d) represent the estimated local thickness maps obtained from the proposed SRB-LWE algorithm and from the traditional LWE implementation [23], respectively. For the traditional LWE, a 5-cycle Hanning windowed sine excitation with center frequency 175 kHz was employed, and the algorithm's parameters were selected through trial and error. The obtained local wavenumber estimation map is converted to a local thickness map using the relation given by Eq. (4) for *f* = 175 kHz.

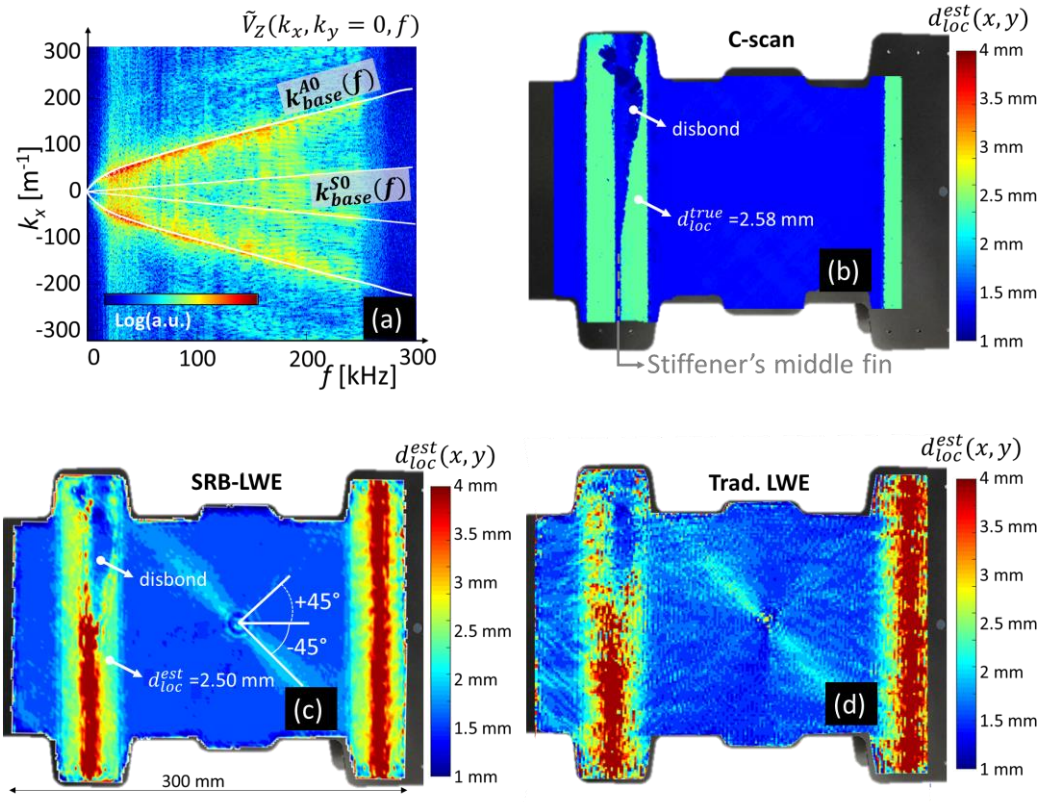

Figure 14: Aircraft CFRP component with disbond at a stiffener: (a) Wavenumber-frequency map for the out-of-plane velocity response along k_y = 0, together with the identified A_0 and S_0 mode curve, (b) C-scan thickness map, (c) SRB-LWE derived thickness map, (d) Traditional LWE [23] derived thickness map.

The estimated local thickness maps obtained through both the traditional LWE and the proposed SRB-LWE algorithms correctly show the extent of the disbond, i.e. where a local thickness is found similar to the thickness of the base material. However, a significant improvement in estimated local thickness

map quality is noticed in the case of SRB-LWE. The improved quality is caused by the superior filter efficiency of using a mode filter (instead of a wavenumber filter), by the averaging effect of employing a broadband approach and by the use of the SNR criterion for frequency frame selection (see also Section 3.4). Because of this high-quality output of SRB-LWE, it is even possible to estimate the local thickness at the non-defected stiffener's area. The found value of d_{loc}^{est} =2.50 mm matches well with the true local thickness d_{loc}^{true} =2.58 mm. Note that a step size of 0.2 mm in the thickness direction was used in the SRB-LWE algorithm.

One may notice small discrepancies in the estimated local thickness maps that are caused by the non-isotropy of the composite material. In between the two stiffeners, the true local thickness is 1.5 mm. However, the estimated local thickness map shows a small increase in estimated thickness in the +45° and -45° directions around the piezoelectric actuator (see Figure 14 (c)). This local thickness increase should be linked to the layup of the laminate. As such, a cross-ply layup with ply angles +45° and -45° is expected. Further, Figure 14 (c) indicates that the bending stiffener is highest in the -45° direction, and to a lesser extent in the +45° direction. Therefore, it may be expected that the outer plies, which contribute most to the bending stiffness, have a -45° angle. This expected cross-ply layup is confirmed after consulting the manufacturer of the aircraft component, who specifies a $[(-45°/+45°)]_{3s}$ layup for the studied component.

4.2.2. Aircraft Panel with BVID

The second aircraft panel has been intentionally impacted with different impact energies of 14 J, 24 J and 21 J in order to induce BVID regions A, B and C, respectively. The inspection is performed in a 2-step way, in order to increase the inspection efficiency. First, a relatively rough SLDV scan, with scan grid spacing of 2 mm, is performed in order to locate possible defects. Second, a more detailed SLDV scan, with dense scan point spacing of 1 mm, is performed on one of the identified hotspots in order to get detailed information on the damage.

Figure 15 (a) shows the out-of-plane velocity response in the wavenumber-frequency domain (along k_y= 0). The identified dispersion curves corresponding to the 4 mm thick base material are indicated. SRB-LWE is performed for the A_0 mode using an evaluated thickness axis: 0.2 mm, 0.4 mm, …, 7 mm. The resulting estimated local thickness map is shown in Figure 15 (b). The three locations of BVID are clearly distinguished as areas of significantly reduced local thickness. Again, the effect of the cross-ply layup is seen close to the excitation locations.

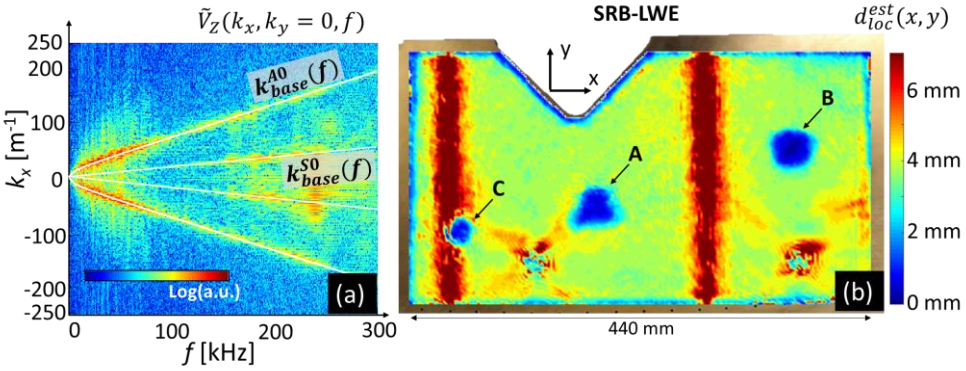

Figure 15: Aircraft CFRP component with 3 areas of BVID: (a) Wavenumber-frequency map for the out-of-plane velocity response along k_y = 0, together with the identified A_0 and S_0 mode curves and (b) SRB-LWE derived thickness map.

In order to accurately quantify the damage hotspot at BVID-B, two additional SLDV scans are performed. The new SLDV scans are focused on the BVID-B region, from the impact side as well as from the backside, and have an increased scan point resolution of 1 mm (see also Table 1). The SRB-LWE derived local thickness maps obtained for the impact- and the backside are shown in Figure 16 (a) and (b), respectively. The local thickness maps obtained using ultrasonic C-scan TOF data are shown in Figure 16 (c) and (d). A high contrast colormap is used to facilitate the comparison of these figures. Overall, a good correspondence is obtained between both inspection methodologies. The different delaminations that make up the BVID, and which are of significant size, can be distinguished in the estimated local thickness map obtained from SRB-LWE. Only the very small delamination fragments cannot be distinguished properly in the SRB-LWE result. In order to detect those with SRB-LWE, even higher frequencies and denser scan grids are required.

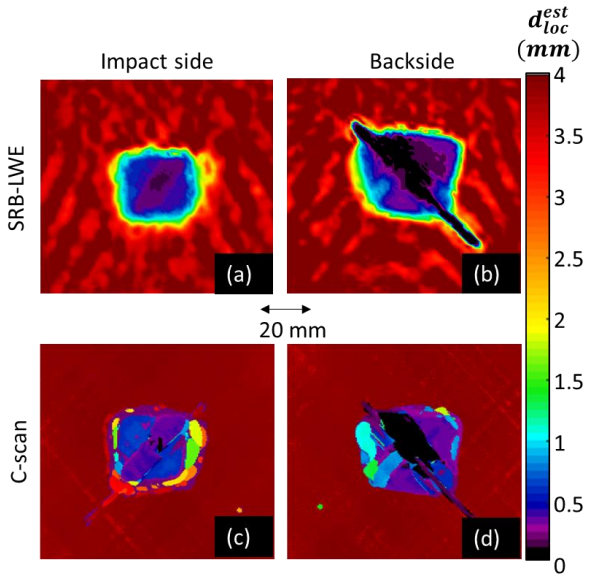

Figure 16: Enlarged view of the estimated local thickness at BVID-B derived from (a,b) SRB-LWE and (c,d) ultrasonic C-scan time-of-flight data. Left column corresponds to *Impact side*, right column to *Backside*.

5. Conclusion

A novel full wavefield inspection method is proposed for damage detection in composite components based on self-reference broadband local wavenumber estimation (SRB-LWE). The procedure results in an estimated local thickness map of the inspected area, in which delamination defects are found as areas of reduced local thickness. The proposed SRB-LWE method uses broadband mode filters in wavenumber-frequency domain, resulting in an improved estimated local thickness map when compared to the thickness map obtained from traditional LWE using narrowband wavenumber filters. The SRB-LWE algorithm is baseline-free, user-independent and does not require the elastic material properties to be known.

Broadband vibrations are introduced in the component using low-power piezoelectric actuators or a pulsed laser. A scanning laser Doppler vibrometer records the full wavefield response. The dispersion curves of the excited Lamb modes are identified in an automated manner, and the A_0 mode is chosen as the mode of interest for further analysis. The A_0 mode curves corresponding to the same material but with different thicknesses are derived under the assumption of isotropic elastic properties. For each of the thickness-specific A_0 mode curves, a broadband filter is constructed in the wavenumber-frequency domain that passes only those vibrations which comply with the thickness-specific A_0 mode curve. The filter characteristics, and corresponding parameter values, are defined in such a way that they remain suited in case the technique is applied on other test specimens. The measurement dataset

is passed through the obtained mode filter bank. At each location of the plate, the filtered dataset is used to calculate the bandpower related to each possible material thickness. The estimated local material thickness is finally obtained as the thickness corresponding to a maximal bandpower density.

The high performance of the SRB-LWE algorithm is verified on three aluminum plates with flat bottom hole defects, and on two cross-ply CFRP aircraft panels with backside stiffeners. The estimated local thickness maps are compared with time-of-flight TOF maps resulting from immersion ultrasound C-scan inspection. The estimated local thickness maps are found to not only reveal the extent of the defects with high precision, but to also give accurate depth estimation of the defects.

Acknowledgments and funding

The authors acknowledge Fonds voor Wetenschappelijk Onderzoek FWO (grant number 1148018N), Bijzonder Onderzoeks Fonds BOF (grant number 01N01719) and the SBO project DETECT-IV (Grant no. 160455), which fits in the SIM research program MacroModelMat (M3) coordinated by Siemens (Siemens Digital Industries Software, Belgium) and funded by SIM (Strategic Initiative Materials in Flanders) and VLAIO (Flemish government agency Flanders Innovation & Entrepreneurship). The authors further thank SABCA Limburg for providing the CFRP aircraft panels.

Declaration of conflicting interests

The authors declared no potential conflicts of interest with respect to the research, authorship and/or publication of this article.

References

1. Nsengiyumva, W., et al., *Advances, limitations and prospects of nondestructive testing and evaluation of thick composites and sandwich structures: A state-of-the-art review.* Composite Structures, 2021. **256**.
2. Rose, J.L., *Ultrasonic Guided Waves in Solid Media*. 2014: Cambridge University Press.
3. Mei, H., et al., *Recent Advances in Piezoelectric Wafer Active Sensors for Structural Health Monitoring Applications.* Sensors (Basel, Switzerland), 2019. **19**(2).
4. Kundu, T., M. Gresil, and V. Giurgiutiu, *Guided wave propagation in carbon composite laminate using piezoelectric wafer active sensors*, in *Health Monitoring of Structural and Biological Systems 2013*. 2013.
5. Jurek, M., et al., *Non-contact excitation and focusing of guided waves in CFRP composite plate by air-coupled transducers for application in damage detection.* Procedia Structural Integrity, 2018. **13**: p. 2089-2094.
6. Truong, C.T., et al., *Comparative Study of Laser Doppler Vibrometer and Capacitive Air-coupled Transducer for Ultrasonic Propagation Imager and the New Development of an Efficient Ultrasonic Wavenumber Imaging Algorithm.* Strain, 2015. **51**(4): p. 332-342.
7. Davies, S.J., et al., *Laser-generated ultrasound: its properties, mechanisms and multifarious applications.* Journal of Physics D: Applied Physics, 1993. **26**(3): p. 329-348.
8. Tola, K.D., et al., *Determination of Plate Corrosion Dimension Using Nd:YAG Pulsed Laser-generated Wavefield and Experimental Dispersion Curves.* Materials (Basel, Switzerland), 2020. **13**(6).
9. Sohn, H., et al., *Noncontact Nonlinear Ultrasonic Wave Modulation for Fatigue Crack and Delamination Detection*, in *Nonlinear Ultrasonic and Vibro-Acoustical Techniques for*

Nondestructive Evaluation, T. Kundu, Editor. 2019, Springer International Publishing: Cham. p. 661-697.
10. Ostachowicz, W., M. Radzieński, and P. Kudela, *50th Anniversary Article: Comparison Studies of Full Wavefield Signal Processing for Crack Detection.* Strain, 2014. **50**(4): p. 275-291.
11. Segers, J., et al., *Backside delamination detection in composites through local defect resonance induced nonlinear source behaviour.* Journal of Sound and Vibration, 2020. **479**.
12. Segers, J., et al., *Nonlinear Elastic Wave Energy Imaging for the Detection and Localization of In-Sight and Out-of-Sight Defects in Composites.* Applied Sciences, 2020. **10**(3924).
13. Segers, J., et al., *Robust and baseline-free full-field defect detection in complex composite parts through weighted broadband energy mapping of mode-removed guided waves.* Mechanical Systems and Signal Processing, 2021. **151**.
14. Radzienski, M., et al., *Damage Identification in Various Types of Composite Plates Using Guided Waves Excited by a Piezoelectric Transducer and Measured by a Laser Vibrometer.* Sensors (Basel, Switzerland), 2019. **19**(9).
15. Keshmiri Esfandabadi, Y., et al., *Full Wavefield Analysis and Damage Imaging Through Compressive Sensing in Lamb Wave Inspections.* IEEE transactions on ultrasonics, ferroelectrics, and frequency control, 2018. **65**(2): p. 269-280.
16. Cuomo, S., et al., *Machine learning for impact detection on composite structures.* Materials Today: Proceedings, 2020.
17. Song, H. and Y. Yang, *Super-resolution visualization of subwavelength defects via deep learning-enhanced ultrasonic beamforming: A proof-of-principle study.* NDT & E International, 2020. **116**.
18. Spytek, J., et al., *Multi-resolution non-contact damage detection in complex-shaped composite laminates using ultrasound.* NDT & E International, 2020. **116**.
19. Sha, G., et al., *Guided wavefield curvature imaging of invisible damage in composite structures.* Mechanical Systems and Signal Processing, 2021. **150**.
20. Wu, Z., S.Y. Chong, and M.D. Todd, *Laser ultrasonic imaging of wavefield spatial gradients for damage detection.* Structural Health Monitoring, 2020.
21. Kudela, P., M. Radzieński, and W. Ostachowicz, *Identification of cracks in thin-walled structures by means of wavenumber filtering.* Mechanical Systems and Signal Processing, 2015. **50-51**: p. 456-466.
22. Kudela, P., M. Radzienski, and W. Ostachowicz, *Impact induced damage assessment by means of Lamb wave image processing.* Mechanical Systems and Signal Processing, 2018. **102**: p. 23-36.
23. Flynn, E.B., et al., *Structural imaging through local wavenumber estimation of guided waves.* NDT & E International, 2013. **59**: p. 1-10.
24. Rogge, M.D. and C.A. Leckey, *Characterization of impact damage in composite laminates using guided wavefield imaging and local wavenumber domain analysis.* Ultrasonics, 2013. **53**(7): p. 1217-26.
25. Michaels, J.E., et al., *Chirp excitation of ultrasonic guided waves.* Ultrasonics, 2013. **53**(1): p. 265-70.
26. Jeon, J.Y., et al., *Damage detection on composite structures with standing wave excitation and wavenumber analysis.* Advanced Composite Materials, 2017. **26**(sup1): p. 53-65.
27. Jeon, J.Y., et al., *2D-wavelet wavenumber filtering for structural damage detection using full steady-state wavefield laser scanning.* NDT & E International, 2020. **116**.
28. Mesnil, O., C.A.C. Leckey, and M. Ruzzene, *Instantaneous and local wavenumber estimations for damage quantification in composites.* Structural Health Monitoring, 2014. **14**(3): p. 193-204.
29. Moon, S., et al., *Optimization of excitation frequency and guided wave mode in acoustic wavenumber spectroscopy for shallow wall-thinning defect detection.* Journal of Mechanical Science and Technology, 2018. **32**(11): p. 5213-5221.

30. Gao, T., et al., *Hidden Corrosion Detection Using Laser Ultrasonic Guided Waves with Multi-frequency Local Wavenumber Estimation.* Ultrasonics, 2020. **108**.
31. O'Dowd, N.M., et al., *Exploring the Performance Limits of Full-Field Acoustic Wavenumber Spectroscopy Techniques for Damage Detection through Numerical Simulation*, in *8th European Workshop on Structural Health Monitoring*. 2016, NDT.net: Bilbao Spain.
32. Juarez, P.D. and C.A. Leckey, *Multi-frequency local wavenumber analysis and ply correlation of delamination damage.* Ultrasonics, 2015. **62**: p. 56-65.
33. Segers, J., et al., *Nonlinear Local Wave-Direction Estimation for In-sight and Out-of-sight Damage Localization in Composite Plates* NDT & E International, 2021. **119**.
34. Sabeti, S. and J.B. Harley, *Spatio-temporal undersampling: Recovering ultrasonic guided wavefields from incomplete data with compressive sensing.* Mechanical Systems and Signal Processing, 2020. **140**.
35. Mesnil, O. and M. Ruzzene, *Sparse wavefield reconstruction and source detection using Compressed Sensing.* Ultrasonics, 2016. **67**: p. 94-104.
36. Di Ianni, T., et al., *Compressive sensing of full wave field data for structural health monitoring applications.* IEEE transactions on ultrasonics, ferroelectrics, and frequency control, 2015. **62**(7): p. 1373-83.
37. Li, Y., et al., *Six-beam homodyne laser Doppler vibrometry based on silicon photonics technology.* Opt Express, 2018. **26**(3): p. 3638-3645.
38. Michaels, T.E., J.E. Michaels, and M. Ruzzene, *Frequency-wavenumber domain analysis of guided wavefields.* Ultrasonics, 2011. **51**(4): p. 452-66.
39. Chang, C.Y. and F.G. Yuan, *Extraction of guided wave dispersion curve in isotropic and anisotropic materials by Matrix Pencil method.* Ultrasonics, 2018. **89**: p. 143-154.
40. Berthaut, J., M.N. Ichchou, and L. Jezequel, *K-space identification of apparent structural behaviour.* Journal of Sound and Vibration, 2005. **280**(3-5): p. 1125-1131.